

赵九江,王哲,张志都,等.利用X射线K吸收边成像法测量碘离子在岩石中的孔隙扩散系数[J].岩矿测试,2023,42(4):667–676.doi:10.15898/j.ykcs.202209050165.

ZHAO Jiujiang, WANG Zhe, ZHANG Zhidu, et al. The Pore Diffusion Coefficient of Iodide Ion in Rock Samples Using X-ray K-edge Imaging[J]. Rock and Mineral Analysis, 2023, 42(4): 667–676. doi: 10.15898/j.ykcs.202209050165.

## 利用X射线K吸收边成像法测量碘离子在岩石中的孔隙扩散系数

赵九江<sup>1</sup>, 王哲<sup>2</sup>, 张志都<sup>2</sup>, 赵鸿<sup>1</sup>

(1. 国家地质实验测试中心, 北京 100037;  
2. 中国科学院高能物理研究所, 北京 100049)

**摘要:** 污染物质在岩层孔隙水中的扩散过程决定了污染物质在地下水与岩层之间迁移的速率, 并进而影响其在环境中的迁移-转化过程。利用碘离子作为示踪剂, 通过X射线成像法可以获得碘离子在岩石中随扩散距离和时间变化的扩散曲线, 进而通过人工拟合获得孔隙扩散系数( $D_p$ )以及孔隙度( $\varphi$ )等重要参数, 这是研究污染元素扩散行为的基础。但是在X射线成像过程中, 岩石本底对X射线的吸收也会对示踪剂碘离子的成像造成干扰。本文使用X射线能谱CT利用X射线K吸收边成像法, 在碘的K吸收边(33keV)两侧的能量区域(27~32keV和34~39keV)对样品进行成像, 有效地减少了岩石背景干扰, 获得碘离子的扩散曲线, 并通过软件利用近似公式对扩散曲线进行拟合获得了灰岩中碘离子的孔隙扩散系数。在实验过程中, 本文还通过改进扩散装置, 对低浓度端溶液采用连续接收的方法, 避免了管路中溶液死体积的影响。通过实验获得碘离子的岩石孔隙扩散系数  $D_p=(1.12\pm0.22)\times10^{-11}\text{m}^2/\text{s}$ , 并计算得到岩石孔隙度  $\varphi=0.02$ 。此实验结果与文献中灰岩孔隙度范围(0.005~0.042)相符合。通过本次工作, 验证了应用改进的扩散装置和X射线K吸收边成像方法测量碘离子在岩石中的孔隙扩散系数的可行性。

**关键词:** X射线能谱 CT; X射线K吸收边成像; 孔隙扩散系数; 碘离子; 灰岩

### 要点:

- (1) 改进了岩石扩散装置, 通过直接接收空白溶液, 减少了管路死体积对岩石孔隙扩散系数测量的影响。
- (2) 利用X射线K吸收边成像方法获得碘离子在灰岩中的扩散曲线, 减少岩石背景干扰。
- (3) 利用互补误差函数的近似公式对碘离子的扩散曲线进行拟合, 获得岩石孔隙扩散系数和孔隙度。

中图分类号: O657.31

文献标识码: A

进入大气、水体、土壤和沉积物等介质中的污染物, 可以通过扩散过程扩大污染面积, 并在不同介质中进行迁移转化, 最终通过食物链进入人体, 进而影响人体健康<sup>[1-6]</sup>, 从而造成复杂且严重的环境问题。进入地下水的污染物在浓度差的推动下通过孔隙水扩散进入岩层, 在此过程中, 污染物可能在岩层中发生反应<sup>[7]</sup>。对污染物进行治理工作之后, 即使地下水中的污染被清除, 存在于岩石孔隙水中的重金属等污染物在浓度差的推动下, 还可以从岩石反向扩散进入地下水中, 形成对地下水的持续污染<sup>[8-11]</sup>。

污染物在岩层中的扩散可以受到很多因素的影响, 如岩层的渗透性、孔隙度、水文地质条件等, 如果岩层具有较高的渗透性和孔隙度, 污染物的扩散速度会更快。研究岩石中元素扩散的方法有许多种, 其中透过扩散法(Through Diffusion)被广泛地获得应用<sup>[12-15]</sup>。在透过扩散法的实验中, 待测元素(示踪剂)从高浓度一侧穿过岩石, 扩散至低浓度一侧, 当达到稳定扩散通量之后, 测量单位时间内穿过岩石的示踪剂的量, 再根据 Fick 第一扩散定律即可计算出扩散系数。阳离子(如金属离子)在岩层中容易被吸附,

收稿日期: 2022-09-05; 修回日期: 2023-03-06; 接受日期: 2023-04-03

基金项目: 国家自然科学基金项目(U1932113)

作者简介: 赵九江, 博士, 副研究员, 从事环境分析化学研究。E-mail: zhaojiujiang@cags.ac.cn。

因此在实际应用中往往利用阴离子如碘离子( $\Gamma$ )或中性分子如超重水(HTO)作为示踪剂<sup>[3,16-18]</sup>。X射线成像方法(X-ray Radiography)被广泛运用于岩石中孔结构表征的研究中<sup>[19]</sup>,它也可以对扩散过程进行研究。不同于透过扩散法,X射线成像法是通过对图像灰度值进行定量化分析<sup>[20]</sup>,对示踪剂如碘离子等较重的原子进行X射线成像,通过软件将图像数值化,利用浓度差别引起的X射线成像灰度变化,获得示踪剂在岩石中的浓度扩散变化曲线。如果初始高浓度端溶液浓度为 $C_0$ ,扩散到某一位置的浓度为 $C_r$ ,那么相对浓度 $C_r/C_0$ 的变化与扩散时间之间存在对应的关系<sup>[12]</sup>,对扩散曲线进行数值拟合,可以获得孔隙扩散系数( $D_p$ ),进而可以计算出有效扩散系数( $D_e=\varphi \cdot D_p$ ,式中 $\varphi$ 为孔隙度)。这种方法在形成稳定扩散通量之前,就可以计算出扩散系数<sup>[12]</sup>。Xiang等<sup>[21]</sup>对乔治亚湾构造岩石样品开展了研究,通过透过扩散法和X射线成像方法获得页岩的有效扩散系数为 $7.0 \times 10^{-13} \text{ m}^2/\text{s}$ 至 $7.7 \times 10^{-12} \text{ m}^2/\text{s}$ ,灰岩的有效扩散系数为 $2.1 \times 10^{-13} \text{ m}^2/\text{s}$ 至 $1.3 \times 10^{-12} \text{ m}^2/\text{s}$ ,泥岩的有效扩散系数为 $5.3 \times 10^{-14} \text{ m}^2/\text{s}$ 至 $5.6 \times 10^{-13} \text{ m}^2/\text{s}$ 。这里的有效扩散系数反映了碘离子从岩石孔隙溶液中扩散出去的能力,它会受到岩石孔的结构、岩石对碘离子的吸附等一系列物理化学环境条件的影响。较高的有效扩散系数说明岩石中碘离子在浓度差驱动下迁移的速率较快。

作为示踪剂的碘元素在岩石中的含量较少,在传统的X射线成像法中,样品中的岩石背景对X射线的吸收依然对碘离子成像有着较大干扰。在实践中,铝制过滤片经常被用来过滤X光机所发射的射线中低能量部分以便减少来自岩石背景的干扰,这同时减弱了X射线的强度,影响了成像效果<sup>[12]</sup>。X射线K吸收边成像的方法,即利用示踪剂在其K吸收边前后X射线衰减系数差异大的特性,选择在示踪剂K吸收边两侧能量区域成像,可以减少岩石背景干扰<sup>[22]</sup>。K吸收边成像可以利用多种方法实现,如两次扫描法,即用不同能量X射线对样品进行连续两次扫描;双源CT法,可以实现同时发射两个能量的X射线,并同时采集两个能量的图像,它需要较为复杂的系统;双层探测器采用了上下两层不同的闪烁晶体材料,在一次常规扫描中,两个能量的X射线吸收系数由上、下层探测器同时获得<sup>[23]</sup>。双能量X射线成像的方法提高了信噪比,因此它在医学、生物以及地质领域都得到了广泛的应用<sup>[24-27]</sup>。最近发展起来的能谱CT,可以通过光子计数探测器(PCDs)

探测并得到X射线光子的能量信息,因此可以在同一位置同时获得X射线K吸收边两侧能量段的图像,并通过数据处理进行物质分解得到吸收边元素的分布<sup>[28]</sup>。在经过K吸收边成像并进行处理后的图像中,其灰度值与示踪剂碘离子浓度呈正相关<sup>[22]</sup>。

本文的研究工作以碘离子为示踪剂,以灰岩为研究对象,使用能谱CT进行X射线K吸收边成像,选择碘元素K吸收边(33keV)两侧的能量区域对灰岩样品进行成像。通过数据处理进行物质分解,从而实现对示踪剂碘离子信号从岩石背景中的有效分离<sup>[22]</sup>。最后通过对图像数据进行拟合,获得灰岩的孔隙扩散系数( $D_p$ )和孔隙度( $\varphi$ )。

## 1 实验部分

### 1.1 扩散实验装置

在研究岩石扩散系数的方法中,通过扩散池(Diffusion Cell)进行透过扩散实验是常用的方法,在以往研究中高浓度示踪溶液与低浓度溶液在各自存储瓶中循环,间隔一段时间测量低浓度端溶液瓶中示踪剂的浓度,同时更换新的空白低浓度溶液<sup>[12,29]</sup>。这样会导致空白溶液中待测元素浓度随采样时间变化,而且管路死体积中溶液所含有的示踪剂会影响扩散系数测量的相对误差<sup>[13]</sup>。本文的研究中使用的本课题组改进后的扩散测量装置(已获得发明专利授权:专利号ZL 2018113023955),可以使空白溶液不返回存储瓶而直接接入样品管进行连续收集,这样一方面尽可能保持待测低浓度端的示踪剂浓度稳定,另一方面可以不必考虑管路中死体积的溶液所含示踪剂的量,使扩散系数测量更加精确。

如图1所示,首先搭建扩散实验装置。岩石样品放置于样品管中,插入样品室上下凸台之间。高浓度碘化钾溶液和空白溶液(去离子水)由蠕动泵(BT100-1L 蠕动泵,保定兰格恒流泵有限公司)泵出,分别进入岩石样品室凸台的下表面和上表面。随后碘化钾溶液泵出样品室返回储存瓶,碘离子在浓度差的驱动下,由下表面扩散到上表面,被空白溶液洗出,间隔一段时间,收集一定量的空白溶液用于测量碘离子浓度。

### 1.2 岩石扩散实验

灰岩样品取自于浙江长兴“金钉子”剖面<sup>[30]</sup>,切割为直径约2.5cm、厚度1~2cm的圆柱体。一共有三个样品:空白参考样品A用去离子水浸泡,用来测量灰岩样品本底的X射线成像灰度值。待测样品B封装进样品管(PVC材质),并将上下两个凸台插入

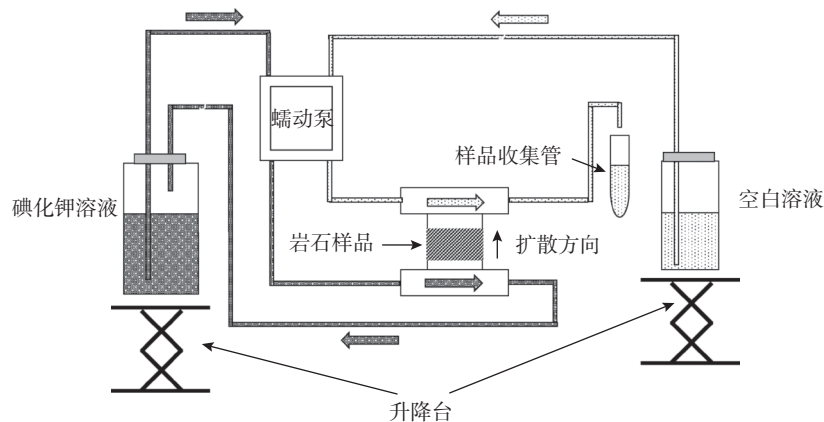


图1 岩石扩散实验示意图

Fig. 1 Experimental set-up for diffusion experiments.

样品管之间,形成样品室,用硅胶密封,然后接入扩散实验装置(图 1)。用于示踪的溶液为碘化钾( $1\text{mol/L}$ ),其中加入少量硫代硫酸钠溶液(纯度 $\geq 99\%$ ,上海麦克林生化科技股份有限公司)作为保护剂,防止碘化钾被空气中氧气氧化。饱和样品 C 用 $1\text{mol/L}$ 碘化钾溶液(纯度 $\geq 99\%$ ,上海麦克林生化科技股份有限公司)浸泡达到饱和(浸泡时间超过两个月),使得碘化钾溶液充满岩石孔隙,用于测量灰岩样品中碘离子最高浓度时刻的 X 射线成像灰度值。空白溶液为去离子水。蠕动泵泵速为 $0.5\text{r/min}$ ,溶液流速约 $6\text{mL/h}$ 。

### 1.3 X 射线 K 吸收边成像实验

实验用的能谱显微 CT 系统由中国科学院高能物理研究所研制组装,能量选择为碘的 X 射线 K 边吸收峰( $33\text{keV}$ )两侧的能量区域( $27\sim 32\text{keV}$  和  $34\sim 39\text{keV}$ ),具体参数由表 1 所示。获取原始图像后,依据前期研究的方法进行 X 射线 K 吸收边成像的数据处理<sup>[22]</sup>。图 2 为 X 射线 K 吸收边成像的示意图,实线和虚线分别代表碘离子和岩石背景对 X 射线的质量衰减系数,在碘离子 K 吸收边( $33\text{keV}$ )附近,碘的衰减系数有一个跳跃的峰值,而相应的岩石成分的衰减系数变化则较为平缓。通过对碘的 K 吸收边左右两侧(阴影区域)的能量范围内的 X 射线分别成像,并用左右两侧成像灰度数据相减,其差值可以消除岩石背景,单独提取出碘元素的信号成分<sup>[22]</sup>。

岩石扩散实验开始后的第 2 天至第 6 天,每天将岩石样品从样品管取出,置于 X 射线能谱 CT 进行 X 射线成像,随后放回样品管继续扩散实验。对于多次 K 吸收边成像的结果进行分析,剔除异常值,通过拟合获得孔隙扩散系数。

表 1 能谱显微 CT 系统成像参数

Table 1 Parameters for X-ray spectral microcomputed tomography (CT) system.

系统参数	测量条件
曝光条件	$90\text{kVp}, 17.28\text{mAs}$
能量阈值设计	$27\sim 32\text{keV}$ 和 $34\sim 39\text{keV}$
光机到探测器距离	$360\text{mm}$
光机到物体距离	$340\text{mm}$
图像像素尺寸	$94.2\mu\text{m/pixel}$

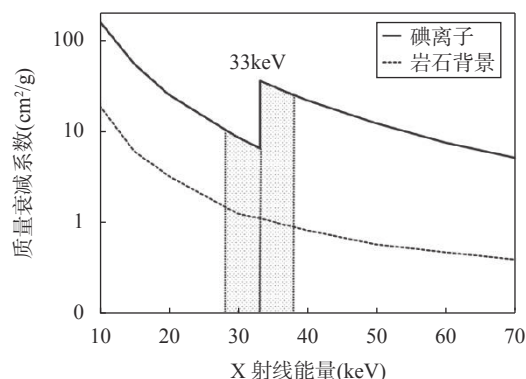


图2 X 射线 K 吸收边成像原理示意图

Fig. 2 Principle diagram of X-ray K-edge imaging.

## 2 结果

### 2.1 透过扩散实验测量岩石有效扩散系数

在进行 X 射线成像实验前,首先利用扩散装置对灰岩样品进行了透过扩散实验。扩散实验采用的样品直径为 $24.74\text{mm}$ ,厚度为 $14.73\text{mm}$ ,高浓度端碘离子溶液浓度为 $1\text{mol/L}$ ,扩散实验开始后 14 天左右达到稳定的扩散速率,在低浓度端采集溶液,并利用 ICP-MS 检测其中的碘离子浓度,根据 Fick 扩散公式,可以计算得到扩散通量<sup>[21]</sup>,进而可以计算出有效扩

散系数为  $D_e = (2.2 \pm 0.7) \times 10^{-13} \text{ m}^2 \text{s}^{-1}$ 。

## 2.2 X射线K吸收边成像法测量岩石孔隙扩散系数

样品 A、B 和 C 的五次取样结果的原始图片通过 imageJ 软件进行数据处理, 将图像转化为 8-bit 灰度图片, 每个像素点的灰度值正相关于岩石孔隙水中的碘离子浓度。通过对样品 B 图像数据处理获得五次扩散采样的相对浓度( $C_t/C_0$ )的扩散变化曲线, 如图 3 所示, 可以看出碘离子相对浓度沿着扩散距离自零点(高浓度溶液端)至空白溶液端呈下降趋势。图 3 中 a 至 e 分别代表第一次至第五次采样获得的碘离子扩散曲线, 随着扩散实验时间的增加, 扩散曲线呈现逐步平直的趋势, 其所形成的扩散曲线满足互补误差函数公式<sup>[12,21,31]</sup>, 如公式(1)所示:

$$\frac{C_t}{C_0} = \operatorname{erfc}\left(\frac{x}{2\sqrt{D_p t}}\right) \quad (1)$$

式中:  $C_t$  为在  $t$  时间, 在  $x$  位置的示踪剂浓度;  $C_0$  为示踪剂起始浓度;  $\operatorname{erfc}$  为互补误差函数;  $x$  为扩散距离;  $D_p$  为孔隙扩散系数;  $t$  为扩散时间。

表 2 为通过拟合获取的孔隙扩散系数, 从结果可以看出, 第一次采样的孔隙扩散系数数据与平均值有较大偏离, 其可能的原因是在扩散实验初始阶段, 碘离子在岩石扩散过程中尚未形成理想的扩散曲线, 因此拟合所得扩散系数偏离较大。通过对第二到第五次采样所得扩散曲线的拟合结果取平均, 所得孔隙扩散系数为  $D_p = (1.12 \pm 0.22) \times 10^{-11} \text{ m}^2/\text{s}$ 。当使用不被岩石本身吸附的示踪剂时, 孔隙扩散系数

与有效扩散系数之间的关系可以用公式:  $D_e = \varphi \cdot D_p$  计算, 其中  $\varphi$  是岩石的孔隙度<sup>[32]</sup>。经过计算得到灰岩样品的孔隙度  $\varphi = 0.02$ 。

## 3 讨论

### 3.1 灰岩有效扩散系数与孔隙度

本文实验结果所得有效扩散系数  $D_e$  为  $(2.2 \pm 0.7) \times 10^{-13} \text{ m}^2/\text{s}$ , 在相关文献报道的灰岩有效扩散系数范围  $5.3 \times 10^{-14} \text{ m}^2/\text{s}$  到  $5.6 \times 10^{-13} \text{ m}^2/\text{s}$  之间<sup>[21]</sup>; 与之相应的本工作所获得的灰岩的孔隙度为 0.02, 也与文献报道的灰岩孔隙度范围(0.005~0.042)相符合<sup>[21]</sup>。这验证了本工作所采用的方法的可行性。通过对比可以看出, 本工作所研究的灰岩具有相对较高的有效扩散系数和孔隙度, 可以使得碘离子以较快的速率通过岩层, 在透过扩散实验中较快地达成稳定的扩散通量。

### 3.2 X射线K吸收边成像方法的改进

在以往 X 射线成像法测量岩石扩散系数研究中, X 射线光源产生能量连续的 X 射线谱, 所产生的图像的灰度反映了透过所有物质的对于能量范围内的 X 射线的平均衰减系数。质量远远多于示踪剂的岩石本底会对相对少量的示踪剂(碘离子)产生较为严重的干扰<sup>[14,21]</sup>。而在本工作中所用的 X 射线 K 吸收边成像方法中, 所选取的能量范围为碘的 K 吸收边两侧, 在此范围内岩石本底与碘离子的衰减系数差异明显, 通过 K 吸收边成像法, 可以有效地分离出示

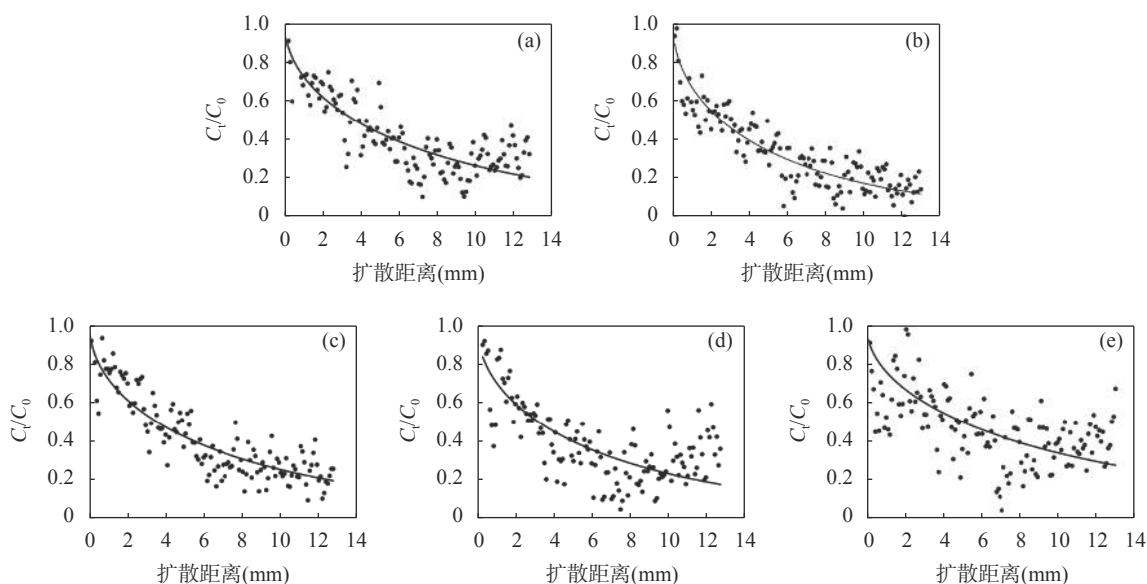


图3 样品 B 中碘离子相对浓度与扩散距离的关系图, 黑色实线为互补误差函数的拟合曲线, 图片编号 a 至 e, 分别代表第一次至第五次实验

Fig. 3 Figures a to e show the relative iodide concentration profiles of sample B for the first to the fifth experiment, respectively. The black solid curves represent the data fitted with an approximate formula of complementary error function.

表 2 X 射线 K 吸收边成像样品孔隙扩散系数的拟合结果

Table 2 The results for the X-ray K-edge imaging data fitting.

采样顺序编号	扩散实验时间 (h)	孔隙扩散系数 $D_p \times 10^{-11} \text{m}^2/\text{s}$
1	42	3.08
2	66	1.19
3	90	1.31
4	119	0.80
5	138	1.20

踪剂碘离子, 提高了信噪比<sup>[22]</sup>。

由于样品几何形状影响, 圆柱形岩石样品边缘薄中心厚, 对 X 射线的吸收随距离中心位置改变而变化, 在中心附近 X 射线被吸收的量(灰度值)变化率最小。因此, 根据空白参考样品 A 径向灰度分布(图 4), 选择中心点附近约±5mm 区间的中心区域灰度值进行计算取平均值, 作为岩石空白本底的灰度值  $Z_{bg}$ , 其对应岩石本底对碘离子浓度的影响  $C_{bg}$ 。同样可以计算碘化钾饱和样品 C 的灰度平均值  $Z_s$ , 所对应的为被碘离子所饱和的岩石孔隙中碘离子的浓度  $C_s$ 。

考虑到岩石样品的不均匀性, 对于待测的扩散样品, 在扩散距离为  $x$  的位置取距离径向中心约±5mm 区间的中心区域灰度值进行平均(对于不同时间采样所获得的图像, 这个范围有少许调整), 所得平均值作为此扩散距离  $x$  的灰度值  $Z_t$ , 所对应的为扩散时间  $t$  时刻的在扩散距离为  $x$  的碘离子浓度  $C_t$ 。则此时刻的相对浓度  $C_t/C_0$  可以通过公式(2)进行计算。

$$\left(\frac{C_t}{C_0}\right)_x = \frac{Z_t - Z_{bg}}{Z_s - Z_{bg}} \quad (2)$$

扩散曲线满足的互补误差函数(公式 1)为非基本函数, 以往在利用 X 射线成像法分析数值化的图像时, 通常通过人工调整参数的方法进行拟合<sup>[21]</sup>, 由此可能产生人为不确定因素。对于误差函数和互补

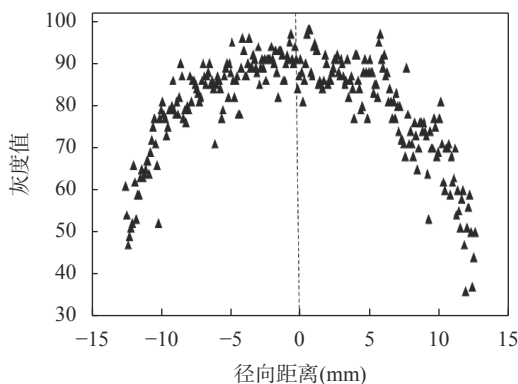


图 4 空白参考样品 A 中 X 射线 K 吸收边成像灰度值 Z 的径向分布

Fig. 4 The radial distribution of grey-scale levels for sample A (blank sample).

误差函数, 有几种简单的近似公式可以进行拟合<sup>[33-35]</sup>, 本次工作经过实际比较, 选用了其中拟合效果较好且相对比较简洁的公式<sup>[34]</sup>作为互补误差函数的近似公式, 进过调整后的近似公式如式(3)所示:

$$\frac{C}{C_0} = 1 - \sqrt{1 - e^{-\frac{4}{\pi} \left( \frac{x}{2\sqrt{D_p t}} \right)^2}} \quad (3)$$

利用公式(3), 对扩散曲线(图 3)通过 SigmaPlot 14 软件进行拟合, 可以获得孔隙扩散系数  $D_p$ , 确保了扩散系数拟合的准确性。

碘离子作为一种惰性示踪剂, 它的化学形态被认为在扩散过程中不发生变化, 且不与岩层发生吸附交换等物理化学反应。而在自然环境中, 碘离子很容易被环境中的氧化性物质氧化为碘酸根离子等<sup>[36-37]</sup>, 碘的扩散系数会发生相应变化<sup>[38]</sup>。在本次研究中, 碘离子溶液中加入保护剂(硫代硫酸钠), 用于抑制空气中氧气对碘离子的氧化, 保证碘离子在扩散过程中不发生化学形态变化。

### 3.3 岩石孔隙扩散系数测量中存在的问题

在进行 X 射线 K 吸收边成像的时候, 需要停止扩散实验, 将样品转移出样品管, 装入 X 射线 CT 机并进行成像。此时岩石两端与高浓度和低浓度溶液断开, 而岩石内部的扩散过程仍然会继续进行, 这导致高浓度端碘离子浓度下降, 而相应的低浓度端的碘离子浓度上升。当 X 射线成像实验结束后, 扩散样品被再次接入扩散装置, 继续扩散实验。实验停止这一段时间内的浓度变化会对整个扩散过程产生一个扰动, 对实验结果产生不可避免的影响。不过, 对于孔隙度和有效扩散系数相对较小的灰岩样品, 上述影响也相对较小。未来的研究中将设计可安置于 X 射线 CT 机中的扩散装置, 希望可以在不中断扩散实验的同时对样品进行成像, 这样避免了扩散实验中断对结果产生的影响。

## 4 结论

本文通过改进扩散测量装置, 并通过 X 射线 K 吸收边成像的方法对碘离子在灰岩样品中的孔隙扩散系数进行测量, 对获得的碘离子在灰岩中的扩散曲线并利用互补误差函数的近似公式进行拟合, 获得岩石的孔隙扩散系数和孔隙度, 验证了方法的可行性。

X 射线 K 吸收边成像的方法与传统的 X 射线成像法相比较, 最大的优点是通过消除岩石本底对示踪剂碘离子的影响, 提高了图像质量, 提供了更加准确的示踪剂的分布, 可以在相对短的时间内实现

了扩散系数的测量。在未来对污染物特别是重金属污染物扩散-迁移-反应的研究中,可以更快地获得污染物的扩散系数,从而更好地评估污染物的污染潜

力,并为采取相对应的措施提供帮助。今后该方法可以应用于岩层孔隙水中的重金属、有机污染物以及放射性核素的迁移及转化的研究中。

## The Pore Diffusion Coefficient of Iodide Ion in Rock Samples Using X-ray K-edge Imaging

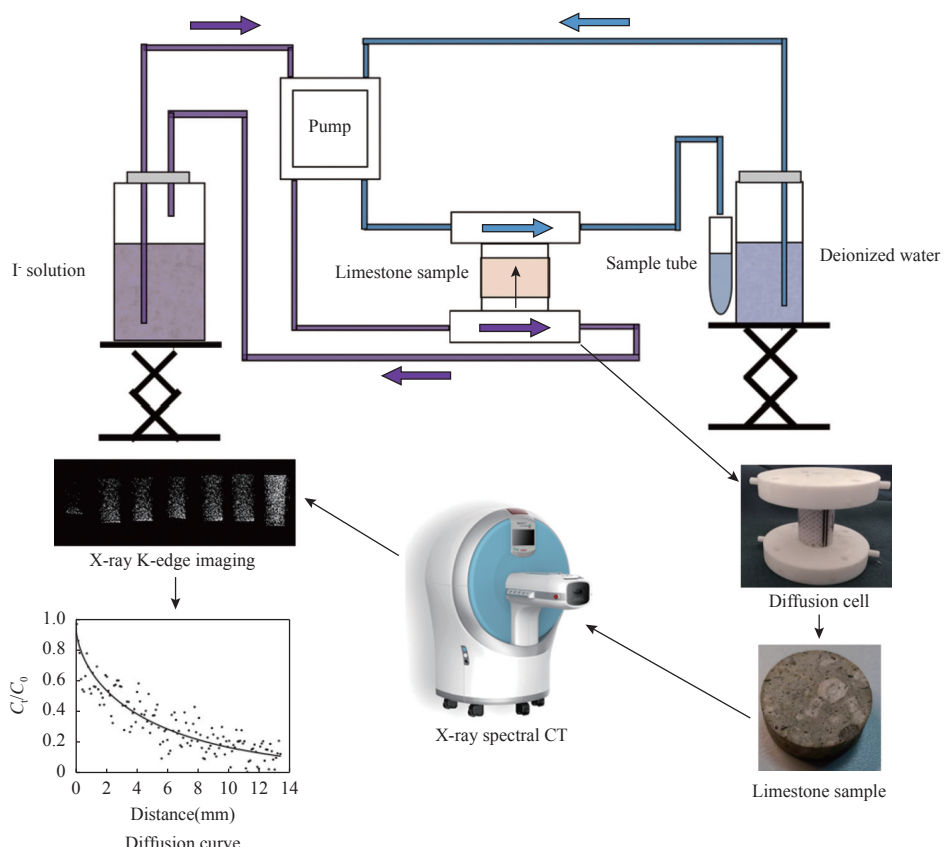
ZHAO Jiujiang<sup>1</sup>, WANG Zhe<sup>2</sup>, ZHANG Zhidu<sup>2</sup>, ZHAO Hong<sup>1</sup>

(1. National Research Center for Geoanalysis, Beijing 100037, China;

2. Institute of High Energy Physics, Chinese Academic of Science, Beijing 100049, China)

### HIGHLIGHTS

- (1) A diffusion experiment device is modified, which can continue to collect low-concentration solution, and prevent interference from dead volume.
- (2) The diffusion curve of iodide ion in limestone samples is obtained by X-ray K-edge imaging to reduce interference from rock background.
- (3) Diffusion data were fitted with an approximate formula of complementary error function to obtain the pore diffusion coefficient and porosity for limestone samples.



## ABSTRACT

**BACKGROUND:** The diffusion process is important for environmental studies and pollution monitoring. When contaminants are released into groundwater in the natural environment, they can diffuse into pore water in the rock matrix driven by the concentration gradients. When the contamination source is removed after remediation, the contaminated porewater can be a long-term contamination source to the groundwater in fractures via back diffusion. The diffusion coefficients are the key parameters for the studies of the diffusion-reaction process of contaminants in the environment, especially in natural porous rocks. The diffusion method, which measures the steady-state diffusion flux of non-sorbing tracers, such as  $I^-$  and HTO, has been widely used for the determination of diffusion coefficients. X-ray radiography techniques, which are non-destructive and can monitor temporal changes of tracers in the porous rock medium, have been developed to obtain the pore diffusion coefficients in rock samples by fitting a solution of Fick's second law of diffusion to profiles of  $\Delta\mu$  (the change in the X-ray attenuation coefficient). The value of  $\Delta\mu$  is a function of the mass of a tracer along the X-ray path. However, the X-ray attenuation by the rock matrix interferes with the determination of tracer signals, due to the low concentration of the tracer in the porewaters. The method of X-ray K-Edge imaging using a photon counting detector (PCD), which takes images from the two energy bins on both sides of the theoretical K-edge position of the tracer element and obtains the image subtraction, can be used for the determination of diffusion coefficients to reduce the interferences from the rock background.

This work focuses on the diffusion process of iodide ion in limestone samples. X-ray K-edge imaging with energy-resolved computed tomography (CT) has been employed to image the iodide ion tracer in limestone samples. The energy range is on both sides of the iodine K-edge (33keV) for X-ray K-edge imaging.

**RESULTS: Modification of diffusion device.** In this work, the diffusion device were modified to continuously collect the low-concentration solution (Fig.1), which prevented the interference from the dead volume. The rock samples were placed in sample tubes and inserted between the upper and lower protrusions of the sample cell. A high concentration potassium iodide (KI) solution and a blank solution (deionized water) were pumped into the lower and upper surface of the rock samples, respectively. Driven by a concentration gradient, iodide ion diffused from the lower surface to the upper surface and was washed out by the blank solution. After a certain period of time, sub-samples of blank solution were collected for measuring the iodide ion concentration.

**X-ray K-edge imaging.** The method of X-ray K-edge imaging was applied to obtain the iodide ion tracer diffusion curve in the limestone sample using a spectral computed tomography. The X-ray energy thresholds were set at 27-32keV and 34-39keV (Table 1), which were on both sides of the iodine K-edge position (33keV).

**Diffusion experiments.** The limestone samples, which were collected from Changxing, Zhejiang, China, were cut as cylindrical samples (2.5cm diameter, 1-2cm length). Subsample A, B and C were the blank sample (no iodide tracer), the sample for diffusion experiment, and the tracer-saturated sample (saturated with iodide tracer), respectively. Sample B was mounted in a diffusion cell and then placed on the diffusion experiment device (Fig.1). The iodide solution(KI, 1mol/L)was then circulated in the tracer reservoir and the low concentration solution deionized water)was collected.

**Diffusion coefficient measurements.** The limestone sample was taken out of the diffusion cell for X-ray K-edge imaging in an X-ray spectral CT from the second day after the diffusion experiment was started. The original images were converted into 8-bit grayscale images using ImageJ software, where the grayscale values were correlated with the normalized iodide tracer concentrations ( $C_t / C_0$ ). To minimize the shape effect of cylindrical samples, the average greyscale values, which were selected from the area of  $\pm 5\text{mm}$  to the center of radial direction, were used for calculating the iodide ion pore diffusion coefficient. The normalized concentration ( $C_t / C_0$ ) is a

function of diffusion distance ( $x$ ) and diffusion time ( $t$ ), which has an analytical solution as  $\frac{C_t}{c_0} = \text{erfc}\left(\frac{x}{2\sqrt{D_p}t}\right)$ , where erfc is the complimentary error function and  $D_p$  is the pore diffusion coefficient. The diffusion curve data (Fig.3) were fitted with an approximate formula of complementary error function (Eq.3) using SigmaPlot 14. The results show that the pore diffusion coefficient,  $D_p$ , is  $(1.12\pm0.22)\times10^{-11}\text{ m}^2\text{s}^{-1}$ .

Before starting the X-ray radiography experiment, a through diffusion experiment was conducted on the limestone sample (24.74mm diameter, 14.73mm length). The iodide ion concentration was determined using ICP-MS and the steady-state iodide flux was used to calculate the effective diffusion coefficient,  $D_e$ , based on Fick's first law of diffusion. The effective diffusion coefficient  $D_p$  for limestone samples was  $(2.2\pm0.7)\times10^{-13}\text{ m}^2\text{s}^{-1}$  and porosity  $\varphi$  was 0.02 calculated by  $D_e=\varphi\cdot D_p$ .

**DISSCUSION:** In previous studies on diffusion coefficient measurements in rocks using X-ray radiography techniques, the X-ray source generates a continuous energy spectrum of X-rays, and the grayscale of the resulting image reflects the average attenuation coefficient of X-rays within the energy range passing through all rock matrices. The background of the rock, which is larger in mass than the tracer (iodide ion), can cause significant interference. In this work, the X-ray K-edge imaging method has been used. Within this selected energy ranges on both sides of the iodine K-edge, there is a noticeable difference in the attenuation coefficients between the rock background and iodide ion. The tracer iodide ion can be effectively separated from the rock background, which improves the signal-to-noise ratio.

In previous studies, fitting of the complementary error function has often been done by manual parameter adjustment, which can introduce artificial uncertainties. In this study, a modified diffusion device is used, and an approximate formula of the complementary error function is applied for data fitting. This approach minimizes systematic errors from both the experimental setup and data processing. The iodide ion is easily oxidized in the environment by an oxidant, such as oxygen. This oxidation can lead to changes in the diffusion coefficient of iodide ion. In this work, sodium thiosulfate is added to the iodide tracer solution to prevent the oxidation of the iodide ion.

The relative iodide ion concentration profiles of sample B (Fig.3) show that the iodide concentration is decreased with increasing diffusion distance and the diffusion curve become flat with increasing experimental time.  $D_p$  for the first sampling deviates from the average  $D_p$  values. This can be attributed to the fact that during the initial stages of the diffusion experiment, the iodide ion may not have formed an ideal diffusion curve in the limestone samples. As a result, the diffusion coefficient obtained from diffusion curve fitting deviates significantly.

The  $D_e$  value obtained from this work agrees with previous studies, in which the  $D_e$  value ranges from  $5.3\times10^{-14}\text{ m}^2\cdot\text{s}^{-1}$  to  $5.6\times10^{-13}\text{ m}^2\cdot\text{s}^{-1}$ . Correspondingly, the porosity of the limestone obtained in this study is 0.02, which is consistent with the reported porosity range of limestone in the literature (0.005-0.042). These results validate that this method will be feasible for determining the pore diffusion coefficients and porosities in rock samples. The method development of X-ray K-edge imaging using an X-ray spectral CT provides a method to obtain the pore diffusion coefficients and reduce the interference from the rock matrix.

Since the concentration changes when the experiment is paused for X-ray CT imaging can introduce disturbances to the entire diffusion process, the experimental results can be obviously affected. In future work, diffusion devices might be modified to be placed inside X-ray CT. Therefore, X-ray K-edge imaging of samples can be carried out without interrupting the diffusion process, avoiding any disruptions that may affect the results.

**KEY WORDS:** X-ray spectral computed tomography; X-ray K-edge imaging; pore diffusion coefficient; iodide; limestone

## 参考文献

- [1] 曾远, 罗立强. 土壤中特异性微生物与重金属相互作用机制与应用研究进展[J]. 岩矿测试, 2017, 36(3): 209–221.
- Zeng Y, Luo L Q. Research progress on the application and interaction mechanism between specific microorganisms and heavy metals in soil[J]. *Rock and Mineral Analysis*, 2017, 36(3): 209–221.
- [2] 董志高, 付婷婷, 李磊, 等. 某简易污泥填埋场污染物调查与扩散迁移研究[J]. 科学技术与工程, 2014, 14(32): 1671–1815.
- Dong Z G, Fu T T, Li L, et al. Study on investigation, diffusion and migration of pollutants in a simple sewage sludge landfill[J]. *Science Technology and Engineering*, 2014, 14(32): 1671–1815.
- [3] Luraschi P, Gimmi T, van Loon L R, et al. Evolution of HTO and  $^{36}\text{Cl}^-$  diffusion through a reacting cement-clay interface (OPC paste-Na montmorillonite) over a time of six years[J]. *Applied Geochemistry*, 2020, 119: 104581.
- [4] Courtin-Nomade A, Waltzing T, Evrard C, et al. Arsenic and lead mobility: From tailing materials to the aqueous compartment[J]. *Applied Geochemistry*, 2015, 64: 10–21.
- [5] Cutruneo C M N L, Oliveira M L S, Ward C R, et al. A mineralogical and geochemical study of three Brazilian coal cleaning rejects: Demonstration of electron beam applications[J]. *International Journal of Coal Geology*, 2014, 130: 33–52.
- [6] Liao X, Li Y, Yan X. Removal of heavy metals and arsenic from a co-contaminated soil by sieving combined with washing process[J]. *Journal of Environmental Sciences*, 2016, 41: 202–210.
- [7] Halloran L J S, Vakili F, Wanner P, et al. Sorption- and diffusion-induced isotopic fractionation in chloroethenes[J]. *Science of the Total Environment*, 2021, 788: 147826.
- [8] Parker B L, Cherry J A, Chapman S W. Discrete fracture network approach for studying contamination in fractured rock[J]. *AQUA mundi*, 2012, 3: 101–116.
- [9] Zhao J, Al T, Chapman S W, et al. Determination of hexavalent chromium concentrations in matrix porewater from a contaminated aquifer in fractured sedimentary bedrock[J]. *Chemical Geology*, 2015, 419: 142–148.
- [10] Muniruzzaman M, Rolle M. Impact of diffuse layer processes on contaminant forward and back diffusion in heterogeneous sandy-clayey domains[J]. *Journal of Contaminant Hydrology*, 2021, 237: 103754.
- [11] Chapman S, Parker B, Al T, et al. Field, laboratory and modeling evidence for strong attenuation of a Cr(VI) plume in a mudstone aquifer due to matrix diffusion and reaction processes[J]. *Soil System*, 2021(VI): 408–413.
- [12] Cavé L, Al T, Xiang Y, et al. A technique for estimating one-dimensional diffusion coefficients in low-permeability sedimentary rock using X-ray radiography: Comparison with through-diffusion measurements[J]. *Journal of Contaminant Hydrology*, 2009, 103(1-2): 1–12.
- [13] Xiang Y, Al T. Effect of confining pressure on diffusion coefficients in low-permeability Ordovician sedimentary rocks from the Michigan Basin, Southwestern Ontario [J]. *Journal of Contaminant Hydrology*, 2016, 195: 2003.
- [14] Nunn J A, Xiang Y, Al T A. Investigation of partial water saturation effects on diffusion in shale[J]. *Applied Geochemistry*, 2018, 97: 93–101.
- [15] Loomer D B, Scott L, Al T A, et al. Diffusion-reaction studies in low permeability shale using X-ray radiography with cesium[J]. *Applied Geochemistry*, 2013, 39: 49–58.
- [16] van Loon L R, Soler J M, Jakob A, et al. Effect of confining pressure on the diffusion of HTO,  $^{36}\text{Cl}^-$  and  $^{125}\text{I}^-$  in a layered argillaceous rock (Opalinus Clay): Diffusion perpendicular to the fabric[J]. *Applied Geochemistry*, 2003, 18(10): 1653–1662.
- [17] van Loon L R, Soler J M, Bradbury M H. Diffusion of HTO,  $^{36}\text{Cl}^-$  and  $^{125}\text{I}^-$  in Opalinus Clay samples from Mont Terri: Effect of confining pressure[J]. *Journal of Contaminant Hydrology*, 2003, 61(1-4): 73–83.
- [18] Jaquenoud M, Elam W T, Grundl T, et al. *In-situ* X-ray fluorescence to investigate iodide diffusion in Opalinus clay: Demonstration of a novel experimental approach [J]. *Chemosphere*, 2021, 269.
- [19] 陈维堃, 腾格尔, 张春贺, 等. 页岩纳米有机孔结构表征技术研究进展[J]. 岩矿测试, 2022, 41(6): 906–919.
- Chen W K, Teng G E, Zhang C H, et al. A review of research progress on characterization technology of nano organic pore structure in shale[J]. *Rock and Mineral Analysis*, 2022, 41(6): 906–919.
- [20] Wu Y, Wang D, Wang L, et al. An analysis of the meso-structural damage evolution of coal using X-ray CT and a gray-scale level co-occurrence matrix method[J]. *International Journal of Rock Mechanics and Mining Sciences*, 2022, 152: 105062.
- [21] Xiang Y, Al T, Scott L, et al. Diffusive anisotropy in low-permeability Ordovician sedimentary rocks from the Michigan Basin in Southwest Ontario[J]. *Journal of Contaminant Hydrology*, 2013, 155: 31–45.

- [22] Zhang Z, Zhang X, Hu J, et al. An optimized K-edge signal extraction method for K-edge decomposition imaging using a photon counting detector[J]. *Frontiers in Physics*, 2021, 8: 1–12.
- [23] 李非, 蔡婧婧. 双能量CT成像技术及其标准研究[J]. *中国医疗器械信息*, 2022, 22(9): 10–15.  
Li F, Cai Q Q. Study on dual-energy CT imaging technology and its standard[J]. *China Medical Device Information*, 2022, 22(9): 10–15.
- [24] Iovea M, Oaie G, Ricman C, et al. Dual-energy X-ray computer axial tomography and digital radiography investigation of cores and other objects of geological interest[J]. *Engineering Geology*, 2009, 103(3-4): 119–126.
- [25] Gupta A, Kikano E G, Bera K, et al. Dual energy imaging in cardiothoracic pathologies: A primer for radiologists and clinicians[J]. *European Journal of Radiology Open*, 2021, 8: 100324.
- [26] Zhao T, Li L, Chen Z. Dynamic material decomposition method for MeV dual-energy X-ray CT[J]. *Applied Radiation and Isotopes*, 2018, 140: 55–62.
- [27] Zhou S, Zhu L, You T, et al. In vivo quantification of bone mineral density of lumbar vertebrae using fast kVp switching dual-energy CT: Correlation with quantitative computed tomography[J]. *Quantitative Imaging in Medicine and Surgery*, 2021, 11(1): 341–350.
- [28] Flohr T, Petersilka M, Henning A, et al. Photon-counting CT review[J]. *Physica Medica*, 2020, 79: 126–136.
- [29] Wigger C, van Loon L R. Effect of the pore water composition on the diffusive anion transport in argillaceous, low permeability sedimentary rocks[J]. *Journal of Contaminant Hydrology*, 2018, 213: 40–48.
- [30] 赵鸿, 杜安道, 李超, 等. 浙江长兴“金钉子”灰岩Re-Os富集机制研究[J]. *地质学报*, 2015, 89(10): 1783–1791.  
Zhao H, Du A D, Li C, et al. Enrichment mechanism of Re-Os in limestone from Changxing Permian—Triassic boundary in Zhejiang[J]. *Acta Geologica Sinica*, 2015, 89(10): 1783–1791.
- [31] Bercu G. New refinements for the error function with applications in diffusion theory[J]. *Symmetry*, 2020, 12(12): 1–13.
- [32] Wang B T, Lee C P, Wu M C, et al. Novel method for analyzing transport parameters in through-diffusion tests[J]. *Journal of Environmental Radioactivity*, 2019, 196: 125–132.
- [33] Vedder J D. Simple approximations for the error function and its inverse[J]. *American Journal of Physics*, 1987, 55(8): 762–763.
- [34] 郭俊克, 郭苏凯. 误差函数的有限形式式近似式及其应用[J]. *太原工业大学学报*, 1988, 19(3): 17–24.  
Guo J K, Guo S K. Finite approximate formula of error function and its applications[J]. *Journal of Taiyuan University of Technology*, 1988, 19(3): 17–24.
- [35] 田锦州, 徐乃忠, 李凤明. 误差函数 $\text{erf}(x)$ 近似计算及其在开采沉陷预计中的应用[J]. *煤矿开采*, 2009, 14(2): 33–35.  
Tian J Z, Xu N Z, Li F M. Proximate calculation of error function  $\text{erf}(x)$  and its application in mining subsidence prediction[J]. *Coal Mining Technology*, 2009, 14(2): 33–35.
- [36] MacKeown H, von Gunten U, Criquet J. Iodide sources in the aquatic environment and its fate during oxidative water treatment—A critical review[J]. *Water Research*, 2022, 217: 118417.
- [37] Ye T, Zhang T Y, Tian F X, et al. The fate and transformation of iodine species in UV irradiation and UV-based advanced oxidation processes[J]. *Water Research*, 2021, 206: 117755.
- [38] Neil C W, Telfeyan K, Sauer K B, et al. Iodine effective diffusion coefficients through volcanic rock: Influence of iodine speciation and rock geochemistry[J]. *Journal of Contaminant Hydrology*, 2020, 235: 103714.